Open Ceramics 7 (2021) 100155

Contents lists available at ScienceDirect

Open Ceramics

journal homepage: www.editorialmanager.com/oceram

Microwave-assisted synthesis of nanoscale VO_2 structures

Matthias Van Zele [a], Hannes Rijckaert [a], Laura Van Bossele [a], Davy Deduytsche [b], Lenny Van Daele [c], Emile Drijvers [a], Christophe Detavernier [b], Isabel Van Driessche [a], Klaartje De Buysser [a,*]

[a] Ghent University, Department of Chemistry, SCRiPTS, Krijgslaan 281-S3, 9000, Ghent, Belgium
[b] Ghent University, Department of Solid State Sciences, CoCooN, Krijgslaan 281-S1, 9000, Ghent, Belgium
[c] Ghent University, Department of Organic and Macromolecular Chemistry, PBM, Krijgslaan 281-S4bis, 9000, Ghent, Belgium

ARTICLE INFO

Keywords:
Vanadium dioxide
Thermochromic
Nanomaterial

ABSTRACT

Nanoscaled VO_2 structures were made using a fast microwave-assisted synthesis method in acetophenone as solvent, starting from vanadium pentoxide V_2O_5. Insights in the reaction and purification process were elaborated by attenuated total reflection infrared and nuclear magnetic resonance spectroscopy, which validated the choice of oleyl amine as ligand and acetophenone as solvent. A straightforward heat treatment in inert atmosphere was used to convert the mixture of VO_x (M) and VOOH phases to thermochromically active monoclinic VO_2 (M) nanomaterials. This conversion process was monitored via *in-situ* X-ray diffraction and gave insight in the influence of ethanol and *tert*-butyl hydroperoxide on the crystal structure and morphology, monitored via bright-field transmission electron microscopy. The thermochromic switching was investigated with differential scanning calorimetry showing a latent heat up to 43.34 J/g.

1. Introduction

Large interest goes to smart materials that can lower the energy consumption needed for room temperature control inside buildings. When scrutinizing energy housekeeping of buildings, a large fraction of the overall energy consumption is attributed to cooling, heating and venting of these buildings. Subsequently, a large portion of energy is lost due to poor insulating properties of fenestration, that accounts for approximately 60% of energy loss through the building envelope[1,2]. To indicate the global impact, buildings in general had a final energy usage of 3.060 million tonnes of oil equivalent, leading to direct emissions of 3 $GtCO_2$ in 2018[3]. Consequently, these energy losses in buildings lead to a substantial emission of greenhouse gasses and, correspondingly, a high economical cost[3]. To tackle these issues, the interest for inorganic smart materials that are able to contribute to lower energy consumption for room temperature control in buildings, has grown immensely. Within this scope, smart materials are often referred to as valuable functional materials of choice for energy saving applications in buildings and architecture[4–6].

Smart materials undergo a reversible change in physical properties as a response to external stimuli such as an external electric or magnetic field, illumination[7,8], altering temperature[9] or pH[10]. The response to such stimuli varies as materials can change physical shape, but also color or mechanical properties can be altered. Even materials that are able to generate an electric potential upon illumination[11,12] or heating[13,14] are classified as smart materials. A large subdivision of these smart materials are labelled as chromic materials. Chromic materials exhibit a change in color, when subjected to various conditions. Photochromic materials for example, undergo this change by interaction with light[15]. Electrochromic materials show a difference in color when applying an electric potential[16–18]. Thermochromic materials on the other hand, show different colors upon temperature variations. Combinations between various responses are possible as some materials combine photochromic and thermochromic properties[19].

Vanadium oxide (VO_2) with a valence state V (+IV) is a promising thermochromic material, which undergoes a reversible metal-insulator transition (MIT) at a critical temperature T_c of ~68 °C, which is relatively low and feasible for window applications. Below this T_c, VO_2 resides in a monoclinic crystal lattice (VO_2 (M), $P2_1/c$) and is transparent for near- and mid-infrared light. Above the T_c, VO_2 (M) phase shifts to a rutile crystal lattice (VO_2 (R), $P4_2/mnm$) and reflects infrared light. This change in optical properties can be explained by a difference in orientation of the V *3d* orbitals when rearranging the crystal lattice[20–22]. In the monoclinic VO_2 (M) phase, the V *3d* orbitals interact with each other,

* Corresponding author.
E-mail addresses: Laura.VanBossele@ugent.be (L.V. Bossele), klaartje.debuysser@ugent.be (K. De Buysser).

https://doi.org/10.1016/j.oceram.2021.100155
Received 31 March 2021; Received in revised form 18 June 2021; Accepted 22 June 2021
Available online 24 June 2021
2666-5395/© 2021 The Authors. Published by Elsevier Ltd on behalf of European Ceramic Society. This is an open access article under the CC BY-NC-ND license (http://creativecommons.org/licenses/by-nc-nd/4.0/).

leading to both a bonding (π) and anti-bonding (π^*) combination of these orbitals. In the rutile VO_2 (R) phase, this interaction is lost due to the differences in unit cell between the monoclinic VO_2 (M) and rutile VO_2 (R) phase. As a consequence, the V $3d_{||}$ orbitals are non-bonding. Subsequently, the Fermi level is now positioned inside the non-bonding $d_{||}$ and anti-bonding π^* bands[23], and the VO_2 material converts from an insulator to a metallic state[20–22] with altered optical properties.

In current state-of-the-art, VO_2 thin films are deposited by physical [24,25] or chemical methods[26–28], consisting of a deposition step and a following heat treatment. Both methods are not suitable for polymer substrates, as the necessary heat treatment for crystallizing the material after deposition easily exceeds the melting points of common polymer films. On the other hand, chemical methods starting from various reagents as NH_4VO_3[29–31], V_2O_5[32–41] or, more recently, $VO(acac)_2$[26,42–44] are used to synthesize microsized powders that easily exceed 400 nm in size because of the uncontrollable growth. This leads to a major drawback as deposition of these microsized powders unavoidably results in losses in optical transparency due to light scattering in the wavelength range for visible light[45]. To circumvent these optical losses and to broaden the scope of applications of this thermochromic material, nanosized particles synthesized via the solution-based synthesis routes should be aimed for to minimize losses in optical transparency. These solution-based methods have the advantage over physical methods to make use of cheaper and more easily upscalable deposition methods [46–48].

This paper focusses on a novel acetophenone-based synthesis route for VO_2 (M) structures. The precursor material is V_2O_5 with a valence state V (+V), that will be reduced to VO_2 with a valence state of +IV during synthesis. The V_2O_5 precursor material is subjected to a microwave-assisted synthesis technique where limited reaction times are needed when compared to conventional heating techniques[40,49]. The reaction parameters are modified by adding ethanol or a hydroperoxide to the mixture. Ethanol tends to reduce V_2O_5 [50], while adding hydroperoxides leads to formation of the vanadium diperoxo $[VO(O_2)_2]^-$ complex [51]. The effect on the crystallinity of both is looked further into. Subsequently, a mixture of oxygen deficient VO_x (M) and VOOH (VO_x/VOOH) nanoparticles is obtained after the synthesis and is functionalized and purified afterwards. Subsequently, the purified VO_x/VOOH materials are subjected to a heat treatment in an inert atmosphere to obtain monoclinic VO_2 (M) nanocrystals. The influence of reaction parameters on the thermochromic effect is assessed both with in-situ X-ray diffraction (XRD) and differential scanning calorimetry (DSC).

2. Materials and methods

2.1. VO_x/VOOH nanoparticle synthesis

VO_x nanoparticles were synthesized in a CEM Discover SP microwave device. In a typical synthesis, 0.2 mmol of V_2O_5 (Merck, 98.5%) was added to 4 mL acetophenone (Sigma-Aldrich, 99%) in a 10 mL Pyrex® glass reaction vessel with a stirring bar. The reaction mixture was rapidly heated up to 200 °C and kept at that temperature for 1 h. Synthesis conditions were varied by addition of *tert*-Butyl hydroperoxide (*tbhp*, Sigma-Aldrich, approximately. 5.5 mol/L in decane) and ethanol (Chem-lab, 100% HPLC grade) to compare the effect on the morphology. A summary of synthesis conditions is shown in Table 1 (see Table 1).

Table 1
Synthesis parameters of samples presented. For clarity, these will be referenced to with an appropriate synthesis label, depicting the main difference between the samples.

Synthesis label	Acetophenone (mL)	Ethanol (mL)	tbhp (mmol)	V_2O_5 (mmol)
Blank	4	0	0	0.2
tbhp	4	0	2	0.2
EtOH	3.8	0.2	0	0.2
tbhp + EtOH	3.8	0.2	2	0.2

2.2. Purification and functionalization process of VO_x nanoparticles

The as-obtained VO_x/VOOH nanoparticles after microwave-assisted synthesis were precipitated when adding an excess volume (ratio 1:5) of hexane isomers (Carl Roth, ≥95%) as non-solvent, followed by a mild centrifugation at 5000 rpm for 5 min. The supernatant was discarded and the precipitated nanoparticles were subjected to an intermediate drying step under vacuum at room temperature (typically 20 °C). Subsequently, hexane isomers were added to redisperse the nanoparticles with 100 μL oleyl amine (Sigma, 70%) during ultrasonification. To purify the VO_x/VOOH nanosuspension, 3 vol equivalents of acetone (Chem-lab, 99+%) or ethanol, relative to the suspension volume, were added to induce precipitation, followed by centrifugation. This precipitation and resuspending cycle was repeated three times, until no more oleyl amine was present in the supernatant, according to ^{1}H Nuclear Magnetic Resonance (NMR) spectroscopy. After the last cycle, the VO_x/VOOH nanoparticles were dried under vacuum (50 mTorr, room temperature) using a schlenk-line.

2.3. Conversion to monoclinic VO_2 (M) nanocrystals

The composition of the supernatant of the reaction was assessed with gas chromatography – mass spectrometry (GC-MS). A Hewlett Packard 5890 GC coupled to a Hewlett Packard 5989A MS in EI ionization mode was used. The equipped column was a CP-SIL 8CB low bleed MS from Varian, with a length of 60 m, internal diameter of 0.25 mm and a film of 0.25 μm. The column flow was set at a constant helium flow of 0.65 mL min−1. Inlet temperature was 280 °C. Temperature gradient was set at 3 min 70 °C, 17.5 °C min−1 to 325 °C, 7.43 min at 325 °C. Splitless injection was used. The detected mass range was 40–400 u.

The purified and dried VO_x/VOOH nanoparticle powders were heat treated at 700 °C at a rate of 10 K/min in an inert nitrogen atmosphere. During this heat treatment, structural properties were mapped using *in-situ* X-ray diffraction (XRD). *In-situ* XRD measurements were carried out on a Bruker D8 Discover XRD system equipped with a Cu X-ray source (λ = 1.5406 Å) and a linear X-ray detector. The samples were put on a Si sample cup on heating stage. θ−2θ measurements were carried out in nitrogen at atmospheric pressure at a temperature of 24 °C.

During in-situ XRD measurements, the samples were heated from RT to 700 °C and cooled back to RT at a heating/cooling rate of 10 °C/min. The temperature was measured with a K-type thermocouple and during heating/cooling the samples were subjected to a controlled N_2 flow of 500 sccm.

The as-obtained VO_2 (M) nanocrystal powders were dispersed in ethanol (1 mg/1 mL) via addition of 1 mg polyvinylpyrrolidone (Alfa Aesar, M.W. 40,000) and following ultrasonification[52–54].

2.4. Characterization of VO_2 materials

Attenuated Total Reflection-Fourier Transform Infrared Spectroscopy (ATR-FTIR) were performed on a Perkin-Elmer (Waltham, MA, USA) FT-IR spectrometer spectrum 1000, equipped with a HATR module.

Bright-Field transmission electron microscope (BFTEM) images were taken on a JEOL JEM-2200FS TEM operated at 200 kV and equipped with Cs corrector. The samples were prepared by dripping the nanoparticle suspensions on a 300-mesh holey carbon copper grid.

Differential scanning calorimetry (DSC) was performed on a TA Instruments (Zellik, Belgium) Q2000 DSC device. Samples (5–10 mg) were placed in T_{zero} aluminum sample pans and subsequently sealed using an T_{zero} aluminum lid. The rate was set at 10 °C/min for heating and the 5 °C/min for cooling. Data analysis was performed using TA Instruments' TRIOS software and provided the enthalpy (peak integration) for the studied materials. The critical temperature T_c is calculated as:

$$Tc = \frac{T_1 + T_2}{2}$$

where T_1 and T_2 are endothermic and exothermic transitions respectively.

The NMR data were collected on a Bruker AVANCE II spectrometer operating at a ^{1}H frequency of 500.13 MHz and equipped with a PATXO probe (^{1}H, ^{13}C, and ^{19}F) at 298.2 K. The two dimensional ^{1}H–^{1}H correlation spectroscopy (COSY) and nuclear Overhauser effect spectroscopy (NOESY) were carried out using standard pulse sequences from the Bruker library, cosygpppqf and noesygpphpp respectively. The NOESY mixing time was set to 300 ms with 4096 data points set in the direct dimension and 2048 data points set in the indirect dimension.

3. Results and discussion

3.1. Reaction mechanism during the microwave-assisted synthesis of VO_x/VOOH nanoparticles

After microwave-assisted synthesis, the composition of the supernatant of the reaction was assessed with ATR-IR to determine the additional reaction products. As can be seen in Fig. 1, small peaks next to distinctive acetophenone peaks appear. These peaks can be attributed to benzoic acid, more particular the O–H stretching between 2938 cm^{-1} and 3154 cm^{-1}, the combination band of O–H and C–O vibrations at 1448 cm^{-1} and the C–O stretching of a carboxylic acid at 1264 cm^{-1}.

This gives reasonable indications for the presence of an oxidation step of acetophenone to benzoic acid. This oxidation of acetophenone during microwave-assisted synthesis explains the reduction of the V_2O_5 precursor with a valence state V (+V) to VO_x/VOOH nanoparticles with a valence state of +IV for VO_x and +III for VOOH. The oxidation of acetophenone to benzoic acid has been assumed to be relevant in prior literature for the solvothermal synthesis of metal oxide nanoparticles [55]. With this knowledge, following reaction equation can be proposed.

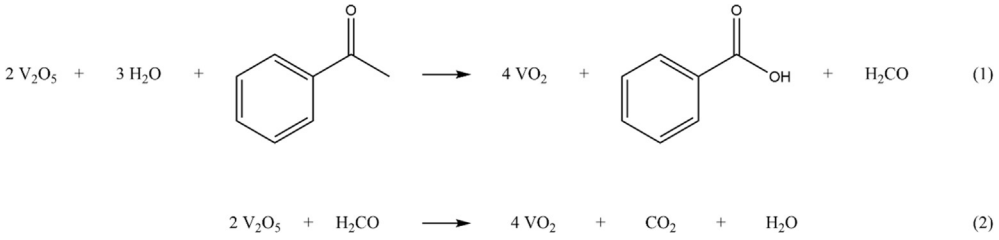

As can be seen in reaction (equation (1)), an initial amount of water is necessary for the reduction of V_2O_5. The necessary water molecules can either originate from the solvent itself, that is not dried before the nanoparticle synthesis and thus contains a minimal amount of water. Another possible source of water molecules can be found in the auto-condensation reaction of acetophenone[56]. GC-MS analysis of the supernatant after synthesis (Fig. 2) detected condensation products of acetophenone, implying that water was formed during the nanoparticle synthesis[56,57]. Note that formaldehyde, formed via reaction (equation (1)), is known to also be able to reduce V_2O_5 (+V) to VO_2 (+IV) via reaction (equation (2)), releasing additional water[58]. This also explains why formaldehyde is not detectable in the supernatant via ATR-IR, as it is readily used during synthesis.

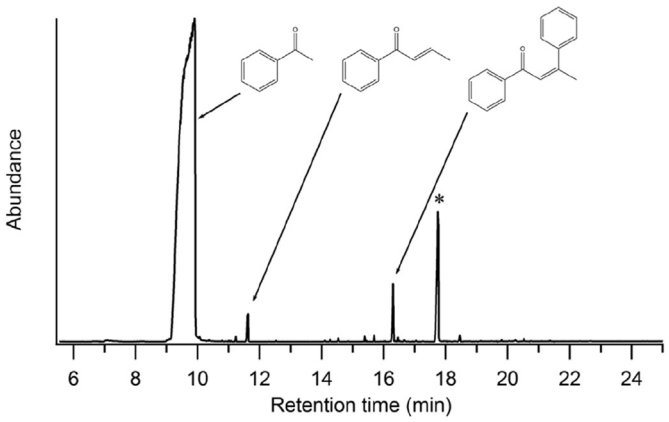

Fig. 2. GC-MS chromatograph of the supernatans after synthesis. The condensation products of acetophenone are indicated at the respective peaks. An additional unidentified compound is detected (*).

3.2. Functionalization and purification of VO_x/VOOH nanoparticles

After microwave-assisted synthesis, a stable suspension of VO_x/VOOH nanoparticles in acetophenone is obtained. In order to obtain phase-pure - VO_2 (M) nanoparticles after heat treatment, the VO_x/VOOH nanoparticles themselves have to be impurity-free. In this work, the VO_x/VOOH nanoparticles are purified and stabilized by long chain alkyl amines as surface ligands in apolar media. Excess organic material is removed by precipitating the nanoparticles with acetone or ethanol as non-solvents and by resuspending them in hexane isomers. The amine of choice is oleyl amine, as the double bond in its long carbon chain gives a distinctive signal in the alkene region of a ^{1}H 1D NMR spectrum (see resonance 4 in Fig. 3A), which allows us to easily assess the surface chemistry of these nanoparticles. Fig. 3A shows the ^{1}H NMR spectrum of

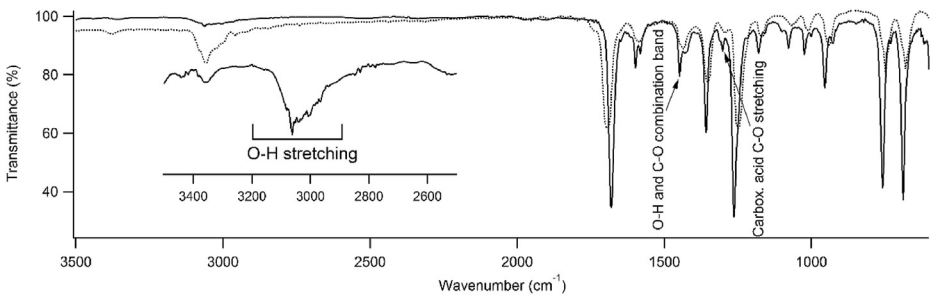

Fig. 1. ATR-IR spectrum of filtered supernatant after reaction of the blank synthesis. When comparing this spectrum to the reference spectrum of pure acetophenone (dotted trace), additional vibrations are found in the broad region between 2900 cm^{-1} and 3200 cm^{-1}, indicating the presence of O–H stretching. At 1448 cm^{-1}, the combination band of O–H and C–O vibrations is found. The C–O stretching for carboxylic acids is indicated at 1264 cm^{-1}. Presence of these vibrations indicates the formation of benzoic acid during synthesis.

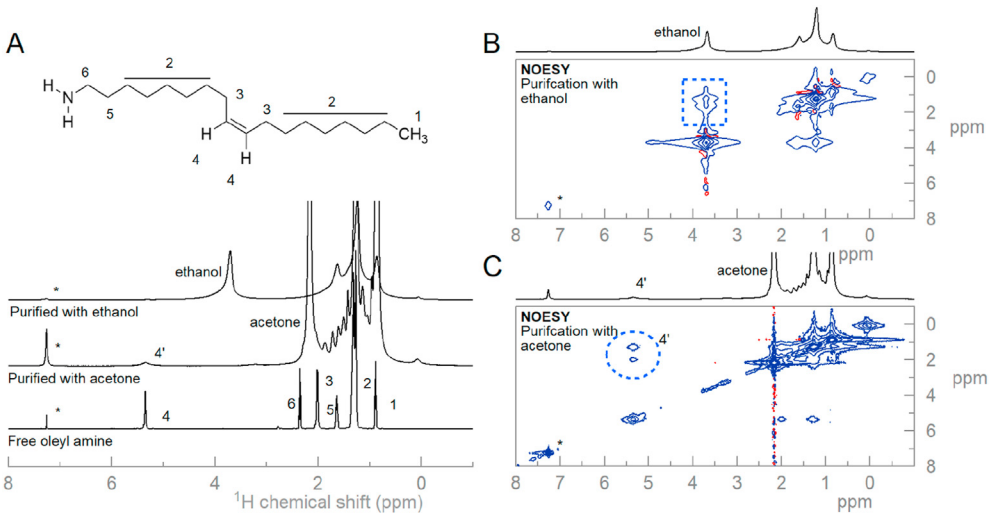

Fig. 3. (A) ^{1}H NMR spectra of (bottom) free oleyl amine dissolved in chloroform-d (*) and the dispersions of the as-synthesized VO_x/VOOH nanoparticles purified with acetone (middle) and ethanol (top) in chloroform-d (*). (B) NOESY spectrum of the as-synthesized VO_x/VOOH nanoparticles purified with ethanol, where the blue square highlights the negative NOE cross-peak and confirms the interaction of ethanol with the nanoparticle surface. (C) NOESY spectrum of the as-synthesized VO_x/VOOH nanoparticles purified with acetone, where the blue circle highlights the negative NOE cross-peak of alkene resonance (4′) of oleyl amine ligand, and thus confirming its presence and interaction with the surface. (For interpretation of the references to color in this figure legend, the reader is referred to the Web version of this article.)

oleyl amine in chloroform-d, which has sharp resonances and therefore indicates that the ligand is free in solution. The nanoparticles which have been purified with acetone show an ^{1}H NMR spectrum with broadened oleyl amine resonances (resonances 4' in Fig. 3A), which strongly suggests that the oleyl amine is interacting with the nanoparticle surface[59,60]. This interaction is further corroborated in the NOESY spectrum, in Fig. 3C, where a strong negative cross-peak of the alkene resonances can be observed in the blue circle. Additionally, while the ^{1}H NMR spectrum show that acetone is still present in solution from the purification process, the NOESY clearly shows no negative cross-peak of the acetone resonances and thus that it does not interact with the nanoparticle surface. In contrast, the nanoparticles which have been purified with ethanol do not show any features of oleyl amine in the ^{1}H NMR spectrum, see Fig. 3A. This result is confirmed in the NOESY spectrum of this sample (Fig. 3B), where the ethanol peak shows a negative cross-peak and therefore indicating that it is interacting with the surface (blue square). This result are not unexpected, as it was already suggested in previous papers that short chains alcohol can exchange with certain ligands and interact with nanoparticle surfaces[61].

According to the covalent bond classification, it can be stated that these VO_x/VOOH nanoparticles interact well with L-type ligands, such as oleyl amine and alcohols[62,63]. Indeed, a swift comparison with literature shows that most often L-type ligands are used during synthesis of VO_x materials[51,64–66]. However, and until now, a clear indication of ligand interaction with the suspended VO_x materials in the literature has been lacking. We therefore conclude that the purification process with oleyl amine as surface ligand and acetone as a non-solvent allows us to produces nanoparticle dispersions with a known and controlled surface

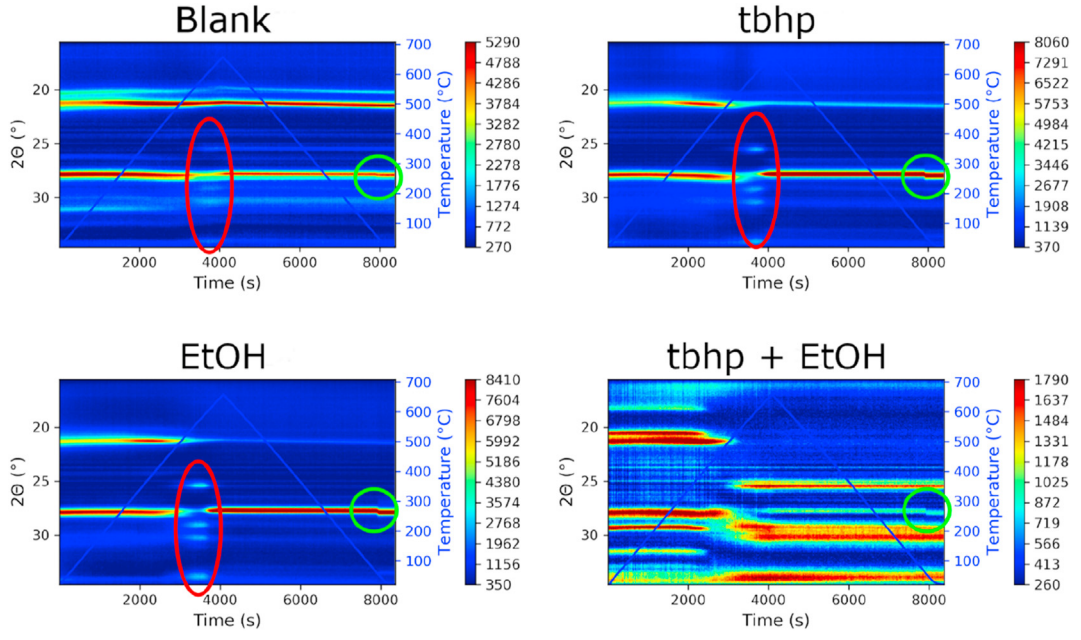

Fig. 4. Overview of *in-situ* XRD measurements. The blue line shows the temperature profile. All samples consist of a mixture of VOx and VOOH phases before heat treatment. The blank, tbhp and EtOH sample are all converted to thermochromically active VO2 (M) phase. This is clearly indicated by the presence of the thermochromic transition around 68 °C in the cooling step (green circle). An intermediate VO2 (B) phase is formed around 650 °C (red circle). For the tbhp + EtOH sample, conversion towards VO2 (B) phase instead of VO2 (M) phase is noted. Compared to the other in-situ diffractograms, a relatively small thermochromic transition is visible. (For interpretation of the references to color in this figure legend, the reader is referred to the Web version of this article.)

chemistry by showing a clear interaction of the oleyl amine ligand with the VO_x/VOOH nanoparticle surface.

3.3. Conversion of VO_x/VOOH nanoparticles to thermochromic VO_2 (M) materials

All obtained VO_x/VOOH nanoparticles via microwave-assisted synthesis were subjected to a heat treatment under inert He atmosphere. During this heat treatment, samples were monitored via *in-situ* XRD. Fig. 4 shows all *in-situ* XRD patterns for the obtained VO_2 structures. The most intense reflections before heat treatment (left hand side of the individual patterns) can be attributed to the VO_2 (M) phase (ICSD 74705) at $2\theta = 27.82$ and VOOH phase (ICSD 76175) at $2\theta = 21.3$. In order to convert this VOOH phase to the thermochromically active VO_2 (M) phase, a heat treatment at 700 °C was necessary. It can be seen that all synthesis products exhibit a transition to an intermediate monoclinic VO_2 (B) phase (ICSD 199, $2\theta = 25.3$, 28.7, 30.2 and 33.9) around 600 °C, indicated by a red circle. This phase on its turn is converted to the rutile VO_2 (R) phase at 700 °C. Sample cooling immediately starts to prevent excessive agglomeration of the crystal structures. Around 68 °C, the rutile VO_2 (R) phase shifts towards the monoclinic VO_2 (M) phase, as can be seen as a small shift where the (110) reflection of the rutile phase changes to the (011) reflection of the monoclinic phase, thus giving a clear first indication of the presence of the thermochromic effect in the material. This transition is marked by the green circle in Fig. 4.

As can be seen in Fig. 4, addition of ethanol or tbhp leads to enhanced crystallinity of the nanocrystals in combination with a reduction of phase impurities, as these signals disappear almost completely. However, addition of both gives rise to structures which are not thermochromically active. According to the diffractogram, the additional reflections present are assigned to monoclinic, non-thermochromic active VO_2 (B). Fig. 5 shows a survey of *ex-situ* diffractograms of all heat treated materials, clearly indicating the presence of the VO_2 (M) phase and some minor impurities. The diffractogram of the tbhp + EtOH product clearly shows that the thermochromically active VO_2 (M) phase is shadowed by the VO_2 (B) phase. For the materials produced in presence of solely tbhp and ethanol, this VO_2 (B) polymorph is present, although less dominant in intensity. The XRD and DSC data are gathered in Table 2.

3.4. Size and morphology of VO_2 materials after heat treatment

Fig. 6 gives an overview of BFTEM images of the synthesized VO_2 (M) materials after heat treatment. One can clearly see that both the blank synthesis and the material produced in the presence of tbhp, consist of multiple crystallites that were sintered together during heat treatment. Sizes of these particles easily exceed several hundreds of nanometers. When looking at the EtOH synthesis, one sees a mixture of small particles and larger, plate-like structures. The particles are small in size, ranging from 5 nm to 20 nm. The plate-like structures range from 30 nm to over 150 nm. These plates also tend to agglomerate and sinter towards sub-microsized structures. When comparing the EtOH synthesized and the tbhp + EtOH synthesized materials, one sees that the smaller particles are not present in the latter. Patterns of *in-situ* XRD of this tbhp + EtOH synthesized material (Fig. 3) identified the final crystal structure as VO_2 (B) phase, meaning that this (B) polymorph grows preferentially as sheets, which is consistent to literature[67]. While VO_2 (B) nanosheets are interesting for electrochemical applications[68,69], however, the focus of this work is the production of thermochromically active VO_2 (M) structures.

3.5. Assessment of thermochromic effect of VO_2 materials after heat treatment

To investigate the thermochromic properties of the materials produced, DSC measurements have been conducted. To compare, enthalpies of commercial VO_2 powders were reported in literature with values

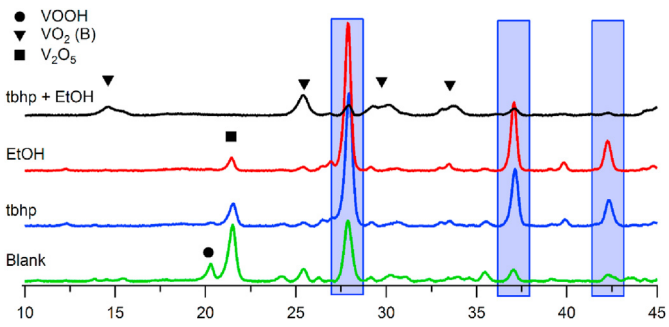

Fig. 5. Comparison of ex-situ XRD diffractograms after heat treatment. The blue regions indicate reflections attributed to VO_2 (M) phase. The EtOH and tbhp samples show only V_2O_5 impurities, while the blank sample also contains unconverted VOOH phase. The tbhp + EtOH sample is primarily converted to VO_2 (B) phase. (For interpretation of the references to color in this figure legend, the reader is referred to the Web version of this article.)

Table 2
Overview of the characterized properties of the materials.

Synthesis label	Crystal phase	Size (nm)	T_c (°C)	Hysteresis (°C)	Latent heat (J/g)
Blank	VOOH, VO_2 (M), V_2O_5	More than 400	–	–	4.12
tbhp	VO_2 (M)	More than 400	63.95	10.16	33.46
EtOH	VO_2 (M)	5-20 (particles) 30 -150 (plates)	64.09	11.11	43.34
tbhp + EtOH	VO_2 (B)	30-150 (plates)	–	–	–

ranging from 39.67 J/g[39] to 41.87 J/g[52]. As can be seen in Fig. 7, the blank sample shows a small thermal transition with a low enthalpy of 4.12 J/g. Upon addition of ethanol or tbhp in the reaction mixture, the thermochromic effect is present more prominently. In case tbhp was added to the particle synthesis, the thermochromic effect showed an enthalpy of 33.46 J/g, which is less than obtained for commercial VO_2 powders. The metal-to-insulator transition (MIT) was detected at 69.03 °C during heating and 58.87 °C during cooling, meaning a critical temperature of 63.95 °C and a hysteresis of 10.16 °C was noted.

When ethanol was present during the particle synthesis, the metal-to-insulator transition was seen at 69.64 °C in the heating run and 58.53 °C in the cooling run. Subsequently, the critical temperature was determined at 64.09 °C and a hysteresis of 11.11 °C was present, similar to the sample produced with tbhp. The enthalpy of the transition however, is higher and amounts to 43.34 J/g, which is more than commercial VO_2 powders. Addition of both tbhp and ethanol leads to a detrimental loss of the thermochromic effect, as was also noted in the diffractogram of the VO_2 material produced (Fig. 3). This means that either ethanol or tbhp is necessary to obtain sufficiently thermochromically active VO_2 (M) phase, while addition of both is detrimental for thermochromic applications. Ethanol reduces V (+V) towards V (+IV) in solvothermal conditions, as is shown in previous literature[29,30,70]. In case of tbhp, the suggestion is that a vanadium diperoxo complex $[VO(O_2)_2]^-$ is formed at the early stage of synthesis, which in its turn is reduced by acetophenone, again producing benzoic acid and formaldehyde. The final product of this reaction cascade is VO_2, as indicated by reaction equations (1) and (2).

4. Conclusion

This work has shown a fast and reliable microwave-assisted synthesis

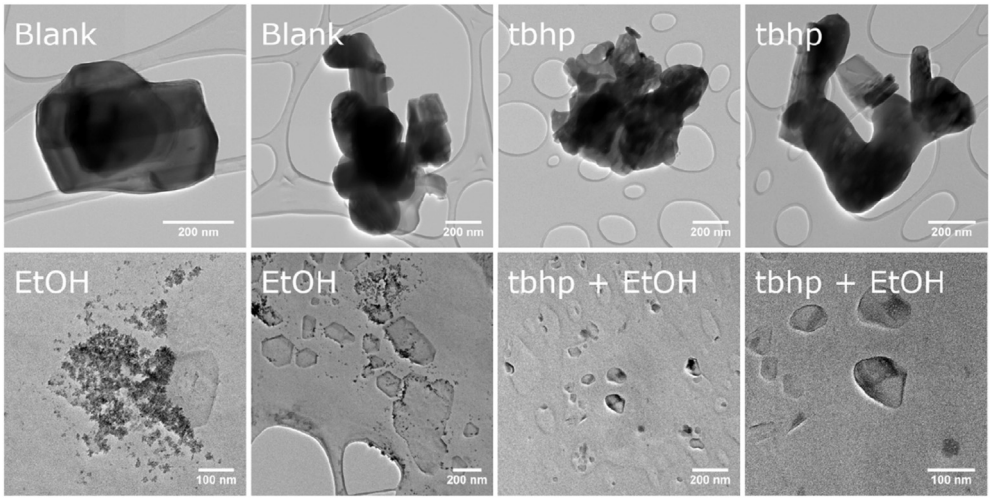

Fig. 6. BFTEM micrographs of heat treated samples. Both the blank and tbhp sample show sintered crystallites. The EtOH sample shows a combination of small VO_2 (M) particles and plate-like VO_2 (B) structures. The tbhp + EtOH sample only shows plate-like structures, attributed to the VO_2 (B) phase.

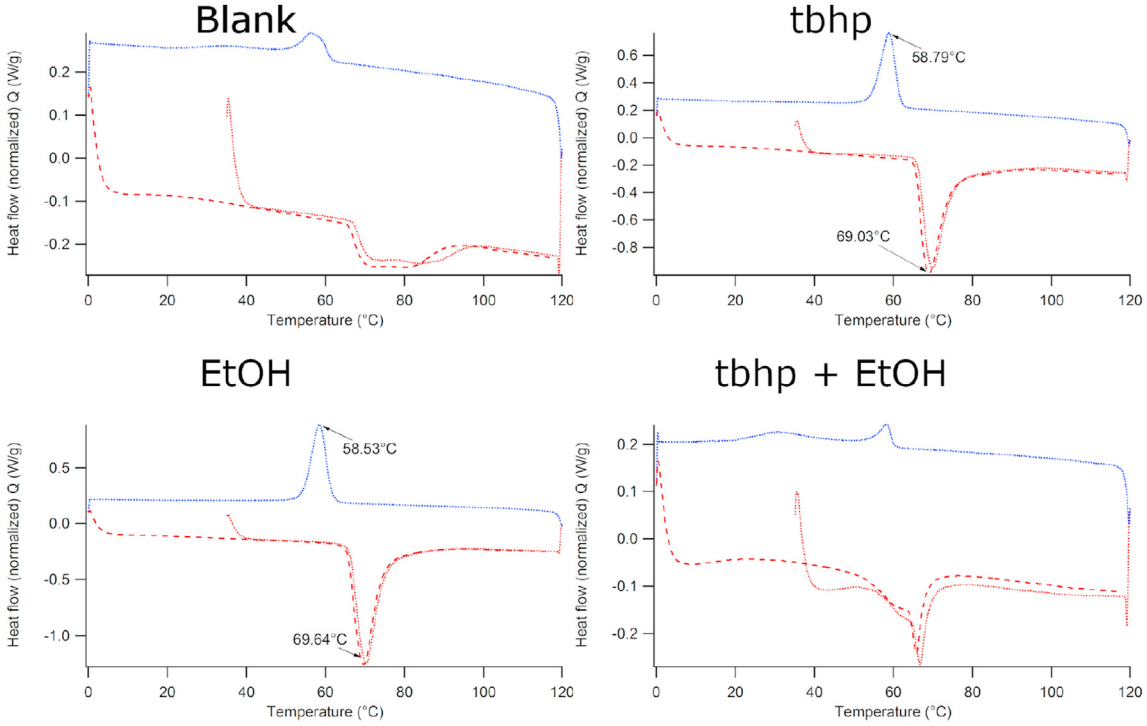

Fig. 7. Comparison of DSC curves after heat treatment. Both the blank and the tbhp + EtOH sample show weak thermochromic transitions, superimposed on broader weak transitions. The tbhp and EtOH samples show reversible thermochromic transitions.

route for VO_2 (M) structures. The purification process was investigated in detail and showed that purification with a combination of long-chain alkyl amines and acetone leads to pure suspensions of VO_x/VOOH materials. Afterwards, a straightforward heat treatment to maximum 700 °C has shown to produce almost phase-pure monoclinic VO_2 materials with varying sizes, as was shown with BFTEM. The influence of different reaction conditions on the thermochromic effect was investigated via *in-situ* XRD and DSC. Results have shown that addition of tbhp leads to the formation of plate-like VO_2 (B) structures, which is interesting for electrochemical applications. On the other hand, via addition of ethanol during the acetophenone synthesis of VO_2 particles, nanometer sized thermochromically active VO_2 (M) structures were obtained. The latent heat of the metal-to-insulator transition reached up to 43.34 J/g according to DSC. However the obtained structures are rather large for optical applications, this paper provides a strong starting point for further optimization towards optical applications.

Conflicts of interest

There are no conflicts to declare.

Declaration of competing interest

The authors declare that they have no known competing financial interests or personal relationships that could have appeared to influence the work reported in this paper.

References

[1] E. Cuce, S.B. Riffat, Vacuum 111 (2015) 83–91.
[2] S.K. Alghoul, H.G. Rijabo, M.E. Mashena, Journal of Building Engineering 11 (2017) 82–86.
[3] IEA, Tracking Buildings, International energy agency, Paris, 2019.
[4] Y.S. Abdullah, H.A.S. Al-Alwan, Ain Shams Engineering Journal 10 (2019) 623–638.
[5] A.S.Y. Mohamed, Energy Procedia 115 (2017) 139–154.
[6] J.W. Yoon, Mater. Sci. Forum 940 (2018) 133–140.
[7] P.-Y. Guo, C. Sun, N.-N. Zhang, L.-Z. Cai, M.-S. Wang, G.-C. Guo, Chem. Commun. 54 (2018) 4525–4528.
[8] R. Wang, X. Lu, L. Hao, W. Jiao, W. Liu, J. Zhang, F. Yuan, F. Yang, J. Mater. Chem. C 5 (2017) 427–433.
[9] K. Connelly, Y. Wu, X. Ma, Y. Lei, Energies 10 (2017) 1889.
[10] B. Cheng, Z. Li, Q. Li, J. Ju, W. Kang, M. Naebe, J. Membr. Sci. 534 (2017) 1–8.
[11] S. Song, Y. Zhang, Y. Xing, C. Wang, J. Feng, W. Shi, G. Zheng, H. Zhang, Adv. Funct. Mater. 18 (2008) 2328–2334.
[12] B. Yuan, X. Liu, X. Cai, X. Fang, J. Liu, M. Wu, Q. Zhu, Sol. Energy 196 (2020) 74–79.
[13] K. Vandaele, B. He, P. Van Der Voort, K. De Buysser, J.P. Heremans, Physical Review Applied 9 (2018).
[14] K. Vandaele, J.P. Heremans, I. Van Driessche, P. Van Der Voort, K. De Buysser, Chem. Commun. 53 (2017) 12294–12297.
[15] J. Zhang, Q. Zou, H. Tian, Adv. Mater. 25 (2013) 378–399.
[16] C.G. Granqvist, M.A. Arvizu, İ. Bayrak Pehlivan, H.Y. Qu, R.T. Wen, G.A. Niklasson, Electrochim. Acta 259 (2018) 1170–1182.
[17] P. Jittiarporn, S. Badilescu, M.N. Al Sawafta, L. Sikong, V.-V. Truong, J. Sci.: Advanced Materials and Devices 2 (2017) 286–300.
[18] P. Yang, P. Sun, W. Mai, Mater. Today 19 (2016) 394–402.
[19] A.M. Kaczmarek, M. Suta, H. Rijckaert, A. Abalymov, I. Van Driessche, A.G. Skirtach, A. Meijerink, P. Van Der Voort, Adv. Funct. Mater. (2020) 2003101, https://doi.org/10.1002/adfm.202003101.
[20] L. Whittaker, C.J. Patridge, S. Banerjee, J. Phys. Chem. Lett. 2 (2011) 745–758.
[21] V. Eyert, Ann. Phys. 11 (2002) 650–704.
[22] J.B. Goodenough, J. Solid State Chem. 3 (1971) 490–500.
[23] S. Shin, S. Suga, M. Taniguchi, M. Fujisawa, H. Kanzaki, A. Fujimori, H. Daimon, Y. Ueda, K. Kosuge, S. Kachi, Phys. Rev. B 41 (1990) 4993–5009.
[24] C. Kang, C. Zhang, L. Zhang, S. Liang, C. Geng, G. Cao, H. Zong, M. Li, Appl. Surf. Sci. 463 (2019) 704–712.
[25] S. Lee, I.N. Ivanov, J.K. Keum, H.N. Lee, Sci. Rep. 6 (2016) 19621.
[26] Ü.Ö.A. Arier, B.Ö. Uysal, Surf. Coating. Technol. 302 (2016) 482–486.
[27] O. Berezina, D. Kirienko, A. Pergament, G. Stefanovich, A. Velichko, V. Zlomanov, Thin Solid Films 574 (2015) 15–19.
[28] N. Wang, Y.K. Peh, S. Magdassi, Y. Long, J. Colloid Interface Sci. 512 (2018) 529–535.
[29] D. Jung, U. Kim, W. Cho, Ceram. Int. 44 (2018) 6973–6979.
[30] H.J. Kim, D.K. Roh, H.S. Jung, D.-S. Kim, Ceram. Int. 45 (2019) 4123–4127.
[31] H. Wu, M. Qin, Z. Cao, X. Li, B. Jia, P. Chen, M. Huang, X. Qu, Chem. Phys. Lett. 706 (2018) 7–13.
[32] L. Dai, C. Cao, Y. Gao, H. Luo, Sol. Energy Mater. Sol. Cell. 95 (2011) 712–715.
[33] Y. Cheng, X. Zhang, C. Fang, J. Chen, J. Su, Z. Wang, G. Sun, D. Liu, Ceram. Int. 44 (2018) 20084–20092.
[34] B. Li, S. Tian, H. Tao, X. Zhao, Ceram. Int. (2018), https://doi.org/10.1016/j.ceramint.2018.11.109.
[35] A. Simo, J. Sibanyoni, X. Fuku, N. Numan, S. Omorogbe, M. Maaza, Appl. Surf. Sci. 446 (2018) 145–150.
[36] D. Verma, D. Singh, P. Kumar, P. Avasthi, V. Balakrishnan, Ceram. Int. 45 (2019) 3554–3562.
[37] S. Wu, S. Tian, B. Liu, H. Tao, X. Zhao, R.G. Palgrave, G. Sankar, I.P. Parkin, Sol. Energy Mater. Sol. Cell. 176 (2018) 427–434.
[38] Y. Zhang, J. Zhang, X. Zhang, S. Mo, W. Wu, F. Niu, Y. Zhong, X. Liu, C. Huang, X. Liu, J. Alloys Compd. 570 (2013) 104–113.
[39] J.M. Booth, P.S. Casey, ACS Appl. Mater. Interfaces 1 (2009) 1899–1905.
[40] A. Gonçalves, J. Resende, A.C. Marques, J.V. Pinto, D. Nunes, A. Marie, R. Goncalves, L. Pereira, R. Martins, E. Fortunato, Sol. Energy Mater. Sol. Cell. 150 (2016) 1–9.
[41] S.R. Popuri, M. Miclau, A. Artemenko, C. Labrugere, A. Villesuzanne, M. Pollet, Inorg. Chem. 52 (2013) 4780–4785.
[42] M. Pan, H. Zhong, S. Wang, J. Liu, Z. Li, X. Chen, W. Lu, J. Cryst. Growth 265 (2004) 121–126.
[43] J.-H. Yu, S.-H. Nam, D. Kim, M. Kim, H.J. Seo, Y.H. Ro, Y.T. Joo, J. Lee, J.-H. Boo, Mater. Res. Bull. 82 (2016) 11–15.
[44] S. Zhang, B. Shang, J. Yang, W. Yan, S. Wei, Y. Xie, Phys. Chem. Chem. Phys. 13 (2011) 15873.
[45] K. Laaksonen, S.Y. Li, S.R. Puisto, N.K.J. Rostedt, T. Ala-Nissila, C.G. Granqvist, R.M. Nieminen, G.A. Niklasson, Sol. Energy Mater. Sol. Cell. 130 (2014) 132–137.
[46] H. Rijckaert, G. Pollefeyt, M. Sieger, J. Hänisch, J. Bennewitz, K. De Keukeleere, J. De Roo, R. Hühne, M. Bäcker, P. Paturi, H. Huhtinen, M. Hemgesberg, I. Van Driessche, Chem. Mater. 29 (2017) 6104–6113.
[47] H. Rijckaert, P. Cayado, R. Nast, J. Diez Sierra, M. Erbe, P. López Dominguez, J. Hänisch, K. De Buysser, B. Holzapfel, I. Van Driessche, Coatings 10 (2019) 17.
[48] M. Van Zele, J. Watté, J. Hasselmeyer, H. Rijckaert, Y. Vercammen, S. Verstuyft, D. Deduytsche, D. Debecker, C. Poleunis, I. Van Driessche, K. De Buysser, Materials 11 (2018) 1101.
[49] H. Rijckaert, J. De Roo, K. Roeleveld, G. Pollefeyt, J. Bennewitz, M. Bäcker, F. Lynen, K. De Keukeleere, I. Van Driessche, J. Am. Ceram. Soc. 100 (2017) 2407–2418.
[50] F. Xu, X. Cao, H. Luo, P. Jin, J. Mater. Chem. C 6 (2018) 1903–1919.
[51] T.D. Nguyen, T.O. Do, Langmuir 25 (2009) 5322–5332.
[52] D. Zomaya, W.Z. Xu, B. Grohe, S. Mittler, P.A. Charpentier, Sol. Energy Mater. Sol. Cell. 200 (2019) 109900.
[53] I.G. Madida, A. Simo, B. Sone, A. Maity, J.B. Kana Kana, A. Gibaud, G. Merad, F.T. Thema, M. Maaza, Sol. Energy 107 (2014) 758–769.
[54] M. Xygkis, E. Gagaoudakis, L. Zouridi, O. Markaki, E. Aperathitis, K. Chrissopoulou, G. Kiriakidis, V. Binas, Coatings 9 (2019) 163.
[55] D. Koziej, M.D. Rossell, B. Ludi, A. Hintennach, P. Novák, J.-D. Grunwaldt, M. Niederberger, Small 7 (2011) 377–387.
[56] K. Saravanan, B. Tyagi, H.C. Bajaj, J. Sol. Gel Sci. Technol. 61 (2011) 275–280.
[57] F. Adam, T.-S. Chew, J. Andas, Chin. J. Catal. 33 (2012) 518–522.
[58] T.E. Ashton, D. Hevia Borrás, A. Iadecola, K.M. Wiaderek, P.J. Chupas, K.W. Chapman, S.A. Corr, Acta Crystallogr. Sect. B Struct. Sci. Cryst. Eng. Mater. 71 (2015) 722–726.
[59] B. Fritzinger, I. Moreels, P. Lommens, R. Koole, Z. Hens, J.C. Martins, J. Am. Chem. Soc. 131 (2009) 3024–3032.
[60] Z. Hens, J.C. Martins, Chem. Mater. 25 (2013) 1211–1221.
[61] N.C. Anderson, M.P. Hendricks, J.J. Choi, J.S. Owen, J. Am. Chem. Soc. 135 (2013) 18536–18548.
[62] M.L.H. Green, G. Parkin, J. Chem. Educ. 91 (2014) 807–816.
[63] J. De Roo, K. De Keukeleere, Z. Hens, I. Van Driessche, Dalton Trans. 45 (2016) 13277–13283.
[64] Y.-H. Jung, S.P. Pack, S. Chung, Mater. Res. Bull. 101 (2018) 67–72.
[65] X. Li, R.E. Schaak, Chem. Mater. 31 (2019) 2088–2096.
[66] T. Paik, S.-H. Hong, E.A. Gaulding, H. Caglayan, T.R. Gordon, N. Engheta, C.R. Kagan, C.B. Murray, ACS Nano 8 (2014) 797–806.
[67] Z. Song, L. Zhang, F. Xia, N.A.S. Webster, J. Song, B. Liu, H. Luo, Y. Gao, Inorg. Chem. Front. 3 (2016) 1035–1042.
[68] C.V. Subba Reddy, E.H. Walker, S.A. Wicker, Q.L. Williams, R.R. Kalluru, Curr. Appl. Phys. 9 (2009) 1195–1198.
[69] J. Ni, W. Jiang, K. Yu, Y. Gao, Z. Zhu, Electrochim. Acta 56 (2011) 2122–2126.
[70] Y. Choi, D.M. Sim, Y.H. Hur, H.J. Han, Y.S. Jung, Sol. Energy Mater. Sol. Cell. 176 (2018) 266–272.